Nanoscale

Accepted Manuscript

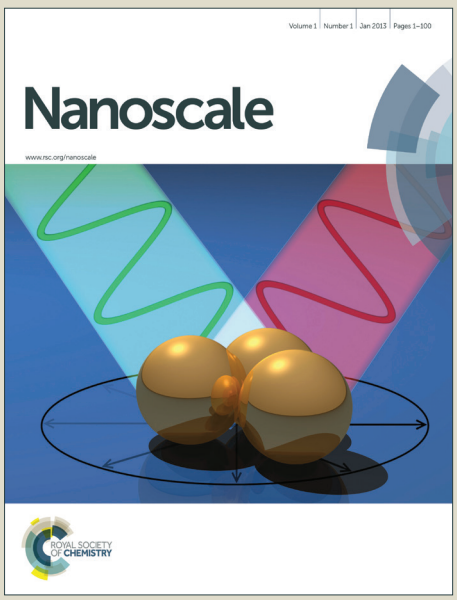

ROYAL SOCIETY OF CHEMISTRY

www.rsc.org/nanoscale

ARTICLE TYPE www. rsc.org/xxxxxx | XXXXXXXX

Vibrational and electronic excitations in gold nanocrystals

Maxime Bayle,[ab] Nicolas Combe,[a] Neralagatta M. Sangeetha,[b] Guillaume Viau,[b] and Robert Carles,[a‡]

Received Xth XXXXXXXXXX 20XX, Accepted Xth XXXXXXXXX 20XX
First published on the web Xth XXXXXXXXXX 200X
DOI: 10.1039/b000000x

An experimental analysis of all the elementary excitations - phonons and electron-holes - in gold nanocrystals has been performed using plasmon resonance Raman scattering. Assemblies of monodisperse, single-crystalline gold nanoparticles, specific substrates and specific experimental configurations have been used. Three types of excitations are successively analyzed : the collective quasi-acoustical vibrations of the particles (Lamb's modes), the electron-hole excitations (creating the so-called "background" in surface-enhanced Raman scattering) and the ensemble of atomic vibrations ("bulk" phonons). The experimental vibrational density of states extracted from the latter contribution is successfully compared with theoretical estimations performed using atomic simulations. The dominant role of surface atoms over the core ones on lattice dynamics is clearly demonstrated. Consequences on the thermodynamic properties of nanocrystals, such as the decrease of the characteristic Debye temperature are also considered.

1 Introduction

Investigating the lattice and electron dynamics and particularly the correlated relaxation processes in metallic nanostructures has been a subject of considerable interest during the last decades as these systems are the building blocks for high frequency opto-electronic devices.[1] In these structures, the coupling between the propagative light (photons) and collective electronic oscillation (plasmons) results in surface plasmon-polariton hybridized modes whose life-time is limited by electron-electron (in the fs scale) and electron-phonon (in the ps scale) interactions.[2]

When the diameter of a metallic nanostructure is lower than 10 nm, the light scattering cross section becomes completely negligible in comparison to the absorption one. Under plasmon resonance conditions, metallic nanocrystals indeed behave as more efficient absorbers than any molecular or quantum-dot systems. Thus, two prominent domains of applications are actually emerging as they take benefit of the short plasmon lifetime and its femtosecond decay in a gas of electron-hole pairs :

(i) electro-plasmonics, where a metallic NC is used as a reservoir of hot electrons and coupled with a semiconductor surface supporting oxydo-reduction reactions,[3]

(ii) thermo-plasmonics, where the transfer of heat from a metallic NC to its environment is exploited.[4]

Moreover, these electron-hole excitations are recognized to play a crucial role in surface enhanced spectroscopies.[5]

The electron-phonon interactions have been particularly investigated using time resolved pump-probe experiments[6,7] or more indirectly using stationary low-frequency Raman spectroscopy, below 1 THz.[8–12] The studies were devoted to coherent elastic waves that imply the nanostructure as a whole (quasi-confined acoustic modes). Indeed, due to phase matching, symmetry selection rules and plasmon resonance effects, the optical response of NCs assemblies in the ps regime is mainly governed by the coupling between coherent collective electronic oscillation and collective atom vibrations. These long wavelength-like vibrations can be analyzed theoretically within the classical elastic theory applied to a continuous medium, following the pioneering work of Lamb.[13] For a sphere, the eigen vibrational modes can be classified according to the principal and azimutal quantum numbers, n and ℓ, respectively. These so-called Lamb's modes are accompanied by a volume and/or shape change of the particle which efficiently modulates the electric susceptibility. Accurate measurements performed on monodisperse gold nanocrystals (Au NCs) have revealed the partial lifting of the $2\ell+1$ spherical degeneracy induced by intrinsic elastic anisotropy.[10,12]

From a general point of view, in noble metals like gold, at room temperature, electrons interact with the whole bath of phonons because the Debye temperature is as low as 170 K.[14] The electron-phonon interactions not only concern the thermalization of hot electrons generated by light excitation, but also electron relaxation processes in transport properties. For thermodynamical properties, it is well known that the thermal capacity is mainly due to phonons because the electronic con-

[a] *Université de Toulouse, CEMES CNRS, 29 rue Jeanne Marvig, BP 94347, 31055 Toulouse Cedex 4, France*
[b] *Université de Toulouse, INSA CNRS UPS, LPCNO, F-31077 Toulouse, France*
‡ To whom correspondence should be addressed. E-mail:carles@cemes.fr

tribution is negligible at room temperature. In a spherical gold particle composed of N_a atoms, $3N_a$ vibrational modes are expected, with $N_a \approx 3000$ for a diameter $D = 5$ nm. Besides few quasi-confined acoustic modes, a majority of these modes are reminiscent of bulk short wavelength ones. These are not sensitive to finite-size effects but give the largest contribution to the vibrational density of states (VDOS). Recording the spectrum of all atomic vibrations in small-size systems is therefore of prime importance, but it has been scarcely achieved because of the effective small cross section for inelastic scattering of photons or neutrons. Until this time no experimental determination of the VDOS in gold nanocrystals (Au NCs) has been performed.

Therefore analyzing these various contributions to the dynamical response of metallic nanostructures, *i.e.* electron-hole excitations, elastic vibrations (Lamb's modes) and surface or bulk phonons, remained a challenge for experimentalists. In this work we exploit specific conditions which allowed to record detailed spectra from a single layer of monodisperse gold nanocrystals (Au NCs). These experimental conditions are presented in Section 2. The results concerning the elastic vibrations of NCs are presented in Section 3. The discrimination of the atomic vibrational contribution from that of the electron-hole excitations (the so-called background in surface-enhanced Raman scattering) is performed in Section 4. Section 5 is devoted to the experimental extraction of the vibrational density of states (VDOS) of Au NCs and to its comparison with various theoretical determinations done by atomic scale simulations. Confinement, surface and strain effects on the dynamical response and consequences on thermodynamical properties are finally discussed.

2 Experiment

The analyzed samples consist of both isolated and assemblies of gold nanocrystals coated by organic ligands and deposited on specific substrates. In order to circumvent the intrinsic limitations due the very low inelastic scattering cross-section and small volume of these Au NPs, an excitation near plasmon resonance, a specific substrate architecture for optical amplification and an original set-up configuration for dark-field-low-frequency Raman spectroscopy have been used.

2.1 Sample characteristics

Citrate stabilized gold nanocrystals were synthesized by the room temperature reduction of an aqueous solution of $HAuCl_4$ by $NaBH_4$ in the presence of trisodium citrate. These nanoparticles were subsequently functionalized with tris(4,6-dimethyl-3-sulfonatophenyl) phosphine (TDSP) ligand. The procedure for the synthesis and surface functionalization are reported in a recent work.[15]. The substrates were first cleaned by rinsing with acetone and then sonicating with ethanol for 10 min. They were then functionalized with amine by immersing in 1% 3-aminopropyl-trimethoxy silane (APTMS) in ethanol for 2 h. They were subsequently rinsed with ethanol, dried under N_2 flow and incubated overnight in an oven at 100°C. For Au NCs deposition, the APTMS coated substrates were immersed in colloidal dispersions for 3 h. The samples were finally rinsed with water and dried under N_2 flow.

A transmission electron microscopy (TEM) image of TDSP-stabilized Au NCs deposited on carbon coated copper grids is shown in Fig. 1a. The low size dispersion allows their self organization in a regular hexagonal lattice, as revealed in one of the insets of Fig. 1a. The Au NCs are crystalline and have an average diameter $D \approx 5.0$ nm (See the other inset of Fig. 1a), with a standard deviation of 15%, as determined by TEM . Similar self-assembled structures obtained from aqueous suspensions of gold NCs protected by TDSP ligands have been recently exploited to fabricate SERS microarrays on silica.[16]

2.2 Plasmon resonance and specific substrates

To counterbalance the weakness of the optical response originating in a small quantity of Au NCs, resonant excitation conditions and optical amplification have been simultaneously fulfilled.[17]

By choosing the laser wavelength λ at the vicinity of the surface plasmon-polariton resonance (SPPR) of the Au NCs, one can take advantage of plasmon resonant enhancement. For an isolated spherical Au NC, the wavelength of the SPPR maximum is more sensitive to the refractive index n of the environment than the diameter D: it evolves from 500 to 520 nm when n changes from 1 (in air) to 1.46 (in silica) with $D = 5$ nm, and from 520 to 530 nm when D changes from 5 to 10 nm in silica. Due to electromagnetic coupling between NCs, the plasmon resonance curve widens and supports a red shift. For self-assembly of TDSP-capped 14 nm diameter Au NCs on silica, the plasmon resonance has been observed near 680 nm.[16] We have chosen $\lambda = 521, 532$ or 638 nm as laser excitation wavelength to take benefit of the vicinity of plasmon resonance condition.

The Au NCs were deposited on specific substrates consisting of a bilayer composed of a thin SiO_2 layer thermally grown on a Si wafer (Fig. 1b). The thickness t of the dielectric layer is adapted to the wavelength of the laser excitation to ensure destructive interference between the waves reflected at the different interfaces. When the reflectance is at minimum, the total electric field reaches its maximum amplitude at the free surface of the bilayer.[17] Therefore, the coupling with NCs deposited on this surface will be amplified. By choosing $t = \lambda/4n = 90$ nm for the thickness of the SiO_2 layer ($n = 1.46$), the optical amplification was tuned near the

plasmon resonance ($\lambda \approx 530$ nm). The energy width of both plasmon-resonance and anti-reflective curves is sufficient to ensure efficient enhancement for the whole (Stokes and anti-Stokes) Raman spectrum due to the small frequency range implied.

2.3 Dark-field and low-frequency Raman spectroscopy

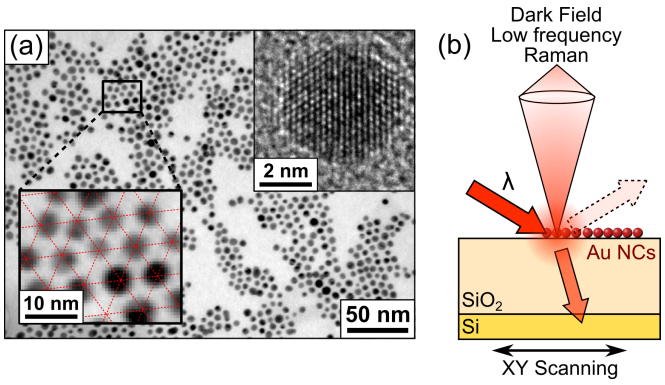

Fig. 1 a) TEM image of a deposit of gold nanocrystals; the enlarged image in the inset (at the bottom) demonstrates the self-organization of these NCs; an example of a high resolution TEM image of a single nanocrystal is shown in the other inset (on top); b) experimental set-up configuration

Collecting a weak inelastic scattered signal in the vicinity of the huge elastic Rayleigh line with a conventional commercial Raman spectrometer is not straightforward. To that purpose, on one hand, we have discarded the usual backscattering geometry with both incident and scattered beams propagating through a unique microscope objective, replacing it by a two objective-system (Fig. 1b): in the resulting dark-field geometry, the specular reflected beam does not enter the spectrometer. On the other hand, the width of the intermediate slit in the spectrometer is chosen to limit the illumination of the CCD detector at the spectral range of interest ($0.12-5$ THz).

A thin layer of Au NCs was used in order to limit diffuse Rayleigh scattering; consequently acquisition times of several minutes and averaging records were necessary to get exploitable signals. The low-frequency Raman spectra in dark-field geometry were recorded with a T64000 Horiba Jobin-Yvon spectrometer equipped with a $\times 100$ entrance microscope objective. Some wide frequency range spectra were recorded using an XploRA Horiba Jobin-Yvon spectrometer. The laser illumination was limited to about $10\mu W/\mu m^2$ to avoid any heating of the sample. This important point was verified using the antiStokes/Stokes ratio as a check (see below).

2.4 Corrected Raman spectra

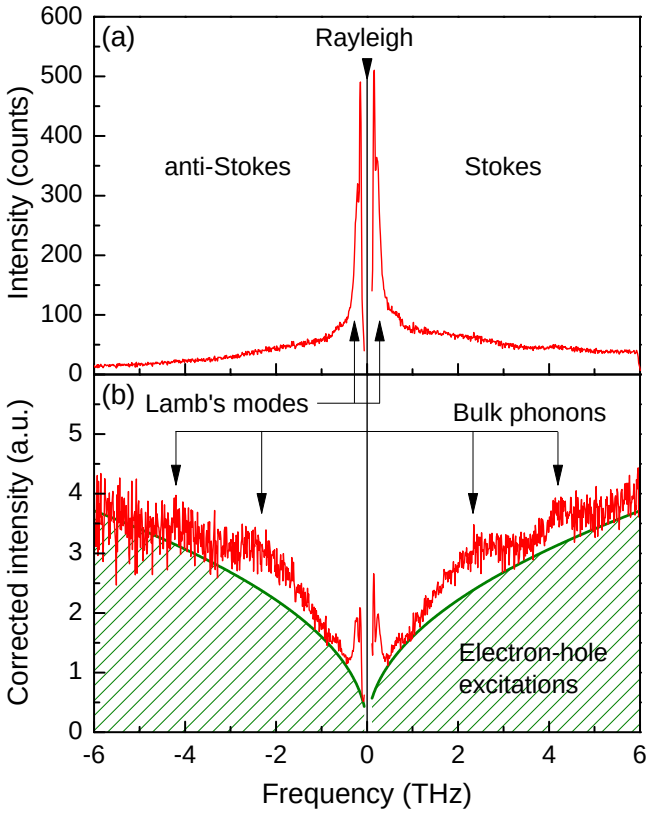

Fig. 2 Low-frequency Raman spectra of the films of gold nanocrystals recorded with $\lambda = 521$ nm, near plasmon resonant conditions on an anti-refractive SiO2/Si layer : a) raw spectrum, b) after response set-up and Bose factor corrections. The ached area shows the electron-hole contribution.

Figure 2a displays the raw Raman spectrum recorded at room temperature on a single layer of Au NCs with a mean diameter of 5 nm. Stokes and antiStokes parts of the inelastic scattering spectrum are shown. They mainly consist in two strong and well-defined peaks at very low frequency ($|\nu| < 1$ THz) with a poorly structured broad tail. In order to extract more reliable information from these data, we have first corrected the raw spectrum from the noise of the CCD detector and from the spectral response of the total set-up by recording the signal of a calibrated white lamp under the same experimental condition. This first correction is particularly important at very low frequency near the detection cut-off around 120 GHz. Second, the resulting signal I is divided by the Bose statistics population factor and one gets the final corrected signal I^{corr} (See Fig. 2b):

$$I^{corr}(\nu) = \frac{I}{|\bar{n}(\nu,T)+1|}\,,\ \bar{n} = \left[\exp\left(\frac{h\nu}{k_B T}\right) - 1\right]^{-1} \qquad (1)$$

where k_B is the Boltzmann constant. This formula applies for both Stokes and anti-Stokes (using $\nu < 0$) parts because $|\bar{n}(-\nu,T)+1| = \bar{n}(\nu,T)$; it applies for all orders of scattering and does not depend on the type of excitations involved, providing the opportunity to discriminate between Raman and photoluminescence processes. In Fig. 2b, despite fluctuations generated in the anti-Stokes region of I^{corr} at large frequency shift where $h|\nu| > k_BT$, one observes the symmetry of the responses for $\nu > 0$ and $\nu < 0$: this demonstrates that the signal as a whole is due to Raman scattering events. This symmetry has been obtained by fixing the temperature T at 305 K, demonstrating that the heating of the sample is negligible. The corrected spectrum $I^{corr}(\nu)$ can be divided into three components:

(i) the low frequency range ($|\nu| < 1$ THz) dominated by the contribution of two well-defined peaks

(ii) a "background" signal monotonously increasing with frequency

(iii) two broad structures centered at $|\nu| \approx 2.4$ and 4.4 THz that are superimposed to the previous background.

We will now successively examine these different contributions to the Raman response.

3 Low frequency range : Lamb modes

Due to confinement, the vibrational spectrum of a NC is discretized at low frequency and an acoustic gap appears. In an isotropic sphere, the vibrational modes are categorized by their angular momentum ($\ell = 0,1,2,\ldots$) and harmonic ($n = 1,2,3,\ldots$) numbers. According to Raman selection rules,[8] spheroidal modes with $\ell = 0$ and 2 are expected in the Raman spectrum. The lowest frequency and most intense peak corresponds to the fundamental quadrupolar ($n = 1, \ell = 2$) mode; it consists in a biaxial contraction/expansion of a planar section of the sphere while the orthogonal direction of the plane is in expansion/contraction. The Raman efficiency of the fundamental spherical mode ($n = 1, \ell = 0$) is lower[18]; it consists in a succession of isotropic extensions/contractions of the whole sphere. This mode is more easily observed in pump-probe experiments[6,7] because it induces a volume change, and thus highly modulates the reflectance. Within the continuous elastic approximation, for an isotropic and homogeneous sphere, a linear dependence of Lamb's mode frequency versus the inverse of the diameter D is predicted:

$$\nu_{n,\ell} = \frac{X_{n,\ell}}{D} \qquad (2)$$

where the different parameters $X_{n,\ell}$ depends on the sound velocities and on the acoustic mismatch between the crystal and embedding medium. Detailed experimental[10,12,19] and refined theoretical analysis[20–22] have shown that the strong elastic anisotropy of gold induces a splitting of the 5-fold degenerate spheroidal $\ell = 2$ modes in a doublet E_g and a triplet T_{2g} (using O_h point group notations). The symmetry of a spherical mode ($\ell = 0$) is not affected (singlet A_g).

The corrected Raman spectrum where the "background" has been subtracted is reported in Fig. 3a. In its low frequency part reported in Fig. 3b, the $E_g - T_{2g}$ splitting is indeed clearly observed: $\nu_{E_g} = 152 \pm 3$ and $\nu_{T_{2g}} = 239 \pm 5$ GHz. One notes, that the intrinsic broadening of the 2-fold degenerated E_g mode (37 GHz) is lower than that of the 3-fold degenerated T_{2g} mode (67 GHz). The observation of the $E_g - T_{2g}$ splitting and the absence of any intermediate "isotropic" signature[11,12] have been considered as a clear demonstration of narrow size distribution and good crystallinity of Au NCs. In Figs 3a and b, one also observes at higher frequency a weaker peak that we assign to the fundamental spherical A_g mode ($n = 1, \ell = 0$) with $\nu_{A_g} = 670 \pm 50$ GHz. To ascertain these assignments, we have calculated the expected corresponding mean diameter D by taking into account the fact that a Lamb's mode frequency always follows the D^{-1} dependence reported in Eq. (2)[20–22]. This has been verified in previous experimental results.[10–12] Thus, using accurate data obtained on free standing Au NCs[20], one has deduced the corresponding $X_{n,\ell}$ parameters: $\nu(\text{GHz}) \times D(\text{nm}) = 746$, 1205 and 3100 for the E_g, T_{2g} and A_g fundamental modes, respectively. Using these values one obtains :$D = 4.97 \pm 0.13$, 5.09 ± 0.10 and 5.4 ± 0.4 nm, respectively, in perfect agreement with the average size deduced from TEM images (5.0 ± 0.8) nm.

4 High frequency range : electronic excitations

4.1 Electronic Raman scattering in metallic NCs

In Fig. 2b the presence of an intense "background" perfectly symmetric in Stokes and anti-Stokes corrected spectra gives evidence of Raman scattering by a continuum of elementary excitations. Such a background is systematically present in SERS spectra and has been attributed to Raman scattering by electron-hole pair excitations.[5,23] Most of these studies focused on SERS substrates containing silver nanostructures. A a comprehensive interpretation of this continuous emission is still awaited for understanding the mechanisms with all the SERS substrates.[24] Very recently, Huang *et al.*[25] have shown that this secondary light emission by Au NCs generated under pulse-laser excitation is due to electronic Raman scattering. These authors have analyzed the thermalization of the excited free electron gas through the intensity decrease of the anti-Stokes emission. In the present work, the coincidence between Stokes and anti-Stokes responses is obtained using $T = 305$ K in the Bose statistics factor, demonstrating that electronic excitations are thermalized near room temperature.

We display in Fig. 4 the Stokes Raman spectrum recorded over a wide frequency scale for two different laser excitation

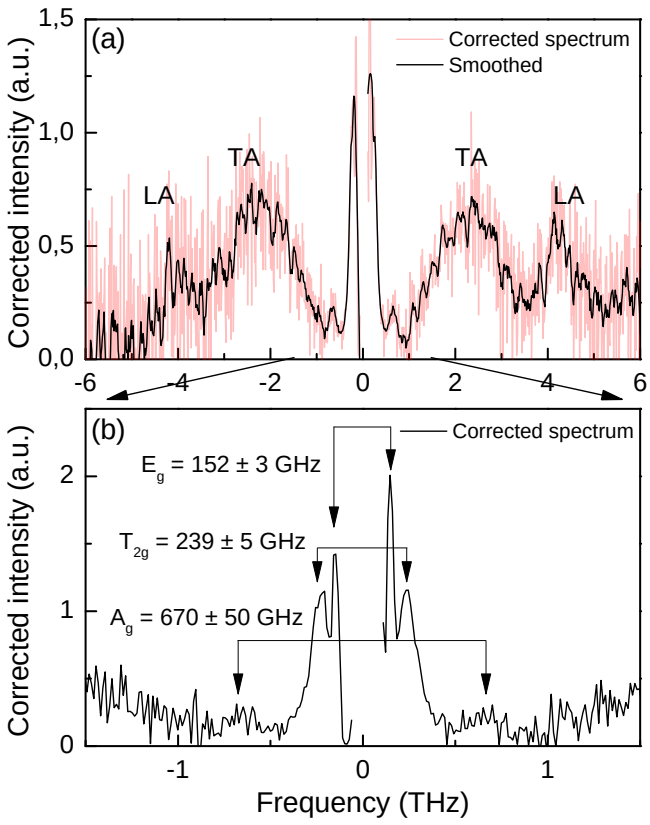

Fig. 3 Low-frequency Raman spectrum of an assembly of Au NCs. The Raman intensity is corrected for Bose's population factor: a) very low frequency part showing the elastic (Lamb's) modes contribution; b) mid-range frequency showing the Au bulk vibrational modes contribution. The signal under the dotted line is attributed to electronic excitations.

wavelengths, 532 and 638 nm. The Raman signal of the Si substrate (first and second order) has been eliminated by substracting the signal originating from a zone without Au NCs (See Fig. 1b). The signal corresponding to 532 nm laser excitation consists in a broad and relatively unstructured wide band. This shape is rather well reproduced by fitting the corrected Raman intensity by the following expression:

$$I_{e-h}^{corr}(\nu) = \frac{I_{e-h}(\nu)}{|\bar{n}(\nu,T)+1|} = I_{max}\frac{2|\nu|\tau}{1+(\nu\tau)^2} \qquad (3)$$

The corrected intensity reaches its maximum I_{max} when the frequency shift equals the scattering rate τ^{-1}. In Fig. 4, this occurs around 41 THz. This modelization is proposed within the theoretical framework on Raman scattering in normal metals containing impurities[26]. In pristine metals, Raman scattering by electrons is forbidden because the wavevector selection rule cannot be fullfilled for creating electron-hole excitations. However the breakdown of this rule through strong electron-phonon interactions was invoked to account for electronic Raman scattering in high-temperature superconductors[27] and recently extended to a large variety of conventional metals[28]. In noble metals like gold, only low energetic acoustical phonons are available and they cannot account for the value of τ^{-1} which is one order of magnitude higher than the phonon cut-off frequency (4.7 THz in gold).[29] Moreover, contrary to bulk metals[28], the corrected intensity of the electronic Raman scattering in metallic NCs is rather insensitive to temperature, *i.e.* to the number of phonons. This suggests a geometrical confinement as the origin for the breakdown of the wave vector selection rule: it is attributed to the intrinsic finite size effect and/or surface corrugations in metallic NCs. The value of $\tau \approx 24$ fs deduced from the spectrum reasonably agrees with the order of magnitude of the electron "collision time" in a nanostructure. As can be seen in Fig. 4, the fit of the background spectrum for Au NCs displays some discrepancy. This may be due to a weak contribution of luminescence processes corresponding to interband radiative recombination of electrons in the *sp* conduction band with holes in the *d* band, as already observed in Au NCs.[30–32]

4.2 SERS effect on the ligands

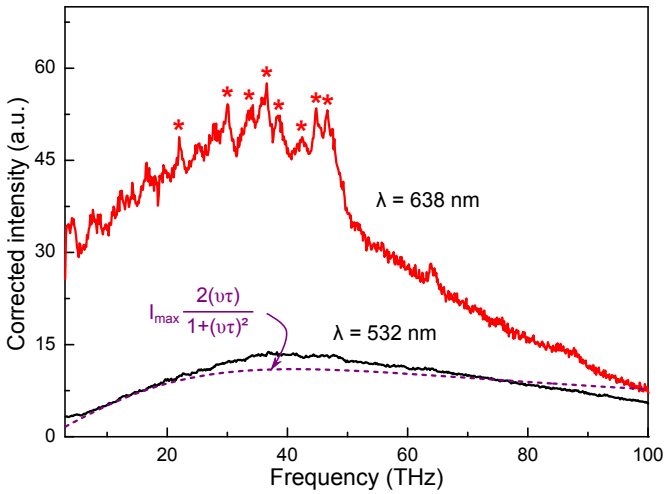

Fig. 4 (Color online) Raman spectra over a wide frequency range of an assembly of Au NCs obtained with near-resonant (black curve at bottom) and in-resonant (red curve on top) plasmon condition, using the 532 and 638 nm as laser wavelength excitation, respectively. For comparison, the corrected intensities of two spectra have been adjusted in their highest frequency range. Principal signatures originating in ligands vibrations are indicated by stars.[16]

In Fig. 4 the Raman spectrum recorded with the 638 nm laser line nearly corresponds to plasmon resonant conditions of the assembly of Au NCs.[16] The intensity of the electronic contribution is globally enhanced when compared with the

case of an out of resonance 532 nm excitation. The lineshape of the electronic contribution is distorted from the prediction of Eq. (3) mainly at low frequency. This complementary emission may be attributed to hot luminescence because the laser energy coincides with the $sp-d$ transitions at the X point of the Brillouin zone.[25,31] In the resonant spectrum, the background increase is accompanied by the emergence of several Raman peaks. They correspond to a SERS effect on modes of TDSP ligands, as already observed recently by Farcau *et al.*[16] on clusters fabricated by convective self-assembly of similar Au NCs. In Fig. 4 all the different SERS features analyzed by these authors are marked with stars; two other SERS bands are also observed near 64 and 85 THz. Of interest is the fact that the frequency-dependence of the resonance enhancement of molecular vibrations is similar to that of the electronic contribution, as observed by comparing the two spectra recorded out- and in-resonance.

We confirm here the fact that electronic excitations do play a crucial role in SERS effect, as underlined in few recent papers.[24,33] This can account for the prominent enhancement effect due to the presence of corrugations on surfaces of SERS substrates,[34] or to the sharpness of the tip in TERS.[30] The generation of uncorrelated electron-hole excitations after optical excitation are thus favoured because of the rapid loss of the plasmon coherence in these nanostructures.

5 Intermediate frequency range:"bulk" phonons

5.1 Experimental investigation of the VDOS

In the intermediate frequency range, between 1 and 5 THz, the two wide bands located near 2.4 and 4.4 THz in both Stokes and anti-Stokes Raman spectra (Fig. 3a) have never been observed on Au NCs. We ascribe these two bands respectively to TA-like and LA-like bulk phonons of gold which become Raman-active due to finite-size effects.

In bulk single crystalline noble metals, first-order Raman scattering is forbidden due to the drastic wavevector selection rule and the absence of long wavelength optical modes. In a nanocrystal, two new phenomena appear: confinement and lack of translational invariance. On one hand, the electric susceptibility of the confined electron gas can be efficiently modulated by global elastic deformations, leading to inelastic scattering by the corresponding Lamb's modes, as previously discussed in Section 3. On the other hand, the translational invariance is lost for all the vibrational waves because spatial correlations are strictly limited to the NC volume. Spatial correlations are also limited to a nano-sized volume in crystals containing foreign atoms or defects and, as a consequence, Disorder-Activated First-Order Raman Scattering (DAFORS) has been observed[35]. Spatial correlation models (SCM) have been proposed to quantitatively account of this phenomenon for optical phonons.[36] Following the pioneering work of Shuker and Gamon,[37] the entire Stokes and anti-Stokes Raman response of randomly disordered crystals has been expressed as a function of the VDOS, $g(\nu)$, within:[38]

$$I_{vib}(\nu) = C(|\nu|)\frac{\bar{n}(\nu,T)+1}{\nu}g(|\nu|) \quad (4)$$

With the exception of glassy or highly ionic materials, it has been observed that $C(|\nu|)/|\nu|$ in is almost constant, like in covalent semiconductors,[35,38], polymers[39,40] or some transition-metal compounds.[41] This was also rather well verified in nanometer-sized crystals.[42–44] In noble metals with cubic symmetry, like gold, it is also expected that no drastic selectivity occurs in the deformation potential mechanism entering the coupling between electrons and "bulk" phonons. Therefore, taking $C(|\nu|)/|\nu|$ as a constant, the vibrational contribution to the corrected Raman intensity will give a good representation of the VDOS:

$$I_{vib}^{corr}(|\nu|) = I^{corr} - I_{e-h}^{corr} \approx C \times g(|\nu|) \quad (5)$$

where C is a constant.

Figure 5a reports the corrected Stokes Raman spectrum. The "background" has been subtracted using Eq. (3) and its intensity adjusted in order to get $I^{corr} - I_{e-h}^{corr} \approx 0$ for $\nu = 5.5$ THz as beyond this frequency the Raman response remains flat (See ached area in Fig. 2b).

We will now show how this resulting Raman spectrum is indeed a good representation of the VDOS in Au NCs. Figure 5b reports the phonon frequencies in bulk gold along high symmetry directions obtained by Lynn *et al.*[29] using coherent inelastic scattering of neutrons at room temperature (dots with error bars). These authors have used a fourth-neighbor general force model with twelve parameters to calculate phonon dispersion curves in good agreement with the experiment. They have deduced the corresponding VDOS in bulk gold reported in Fig. 5a. The correspondance between Van Hove singularities in this VDOS and high symmetry points (X, L and K) of the Brillouin zone are indicated by dotted lines. The "experimental VDOS" obtained in this work from 5 nm-size Au NCs can be then quantitatively compared to this bulk VDOS by adjusting their integrated area which is simply the number of vibrational modes. At first glance, the similarities between the two spectra is remarkable. In particular the area corresponding to the two-fold degenerated TA-like band is more or less twice that of the LA-like band, testifying that neither polarization (TA or LA) nor frequency-dependence of the electron-phonon coupling is observed experimentally.

However, some discrepancies are observed:

(i) on the TA band, between 0.5 and 2 THz, an excess of modes is observed in the spectrum of NCs.

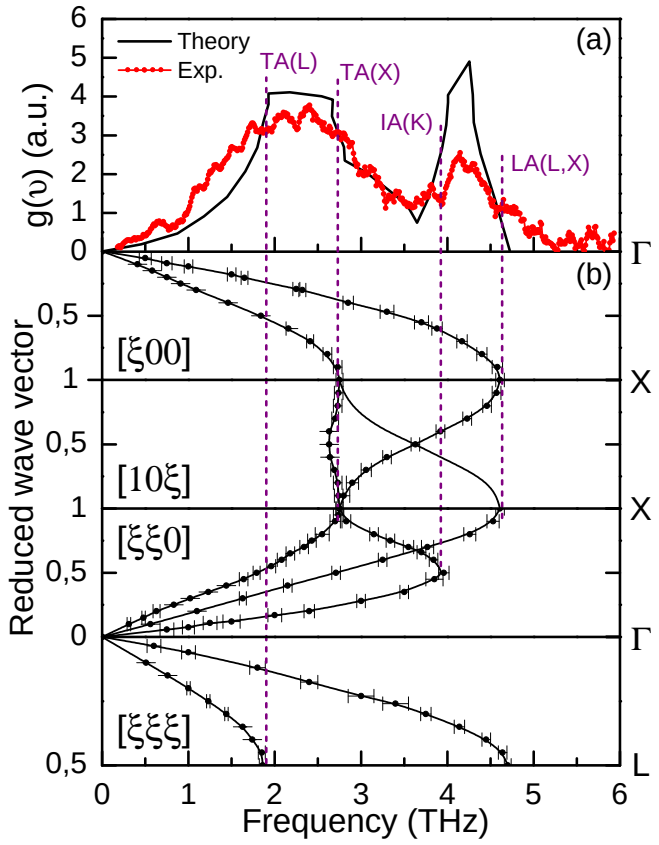

Fig. 5 (a) "Experimental VDOS" obtained in this work using plasmon-resonant Raman scattering (red dotted line) in comparison with theoretical estimations of the VDOS in bulk Au(continuous back line).[29] The arrows indicate phonon frequencies at high symmetry points of the Brillouin zone. (b) Phonon dispersion curves in bulk Au: the dots and errors bars are the experimental data obtained by inelastic neutron scattering.[29] The contribution of the Lamb's modes has been subtracted

(ii) in the highest frequency range, between 3.5 and 4.5 THz, the sharp band corresponding to LA modes in bulk Au is broadened in Au NCs.

(iii) beyond 4.6 THz, corresponding to the cut-off of bulk phonons (LA modes near the L point), an overall shift is observed with a high frequency tail.

These observations are indicative of a frequency redistribution of modes in Au NCs, as theoretically predicted for Ag NCs.[45] On one hand, the "low frequency excess" was attributed to vibrations of under-coordinated surface atoms characterized by a different binding. This can be viewed as a reduction of dimensionality leading to a change on frequency-dependence from quadratic (3D for volume modes) to linear (2D for surface modes) in the Debye approximation. In Fig. 5a, one observes effectively that for $\nu < 1.5$ THz, where the phonon dispersion curves are linear in bulk gold[29] (See Fig. 5b), the VDOS in NCs is in between a linear and quadratic frequency-dependence. On the other hand, the so-called "high frequency tail" was attributed to a stiffening of the chemical bondings between inner atoms due to the contraction of lower coordinated atoms at the surface.

5.2 Comparison with theoretical VDOS

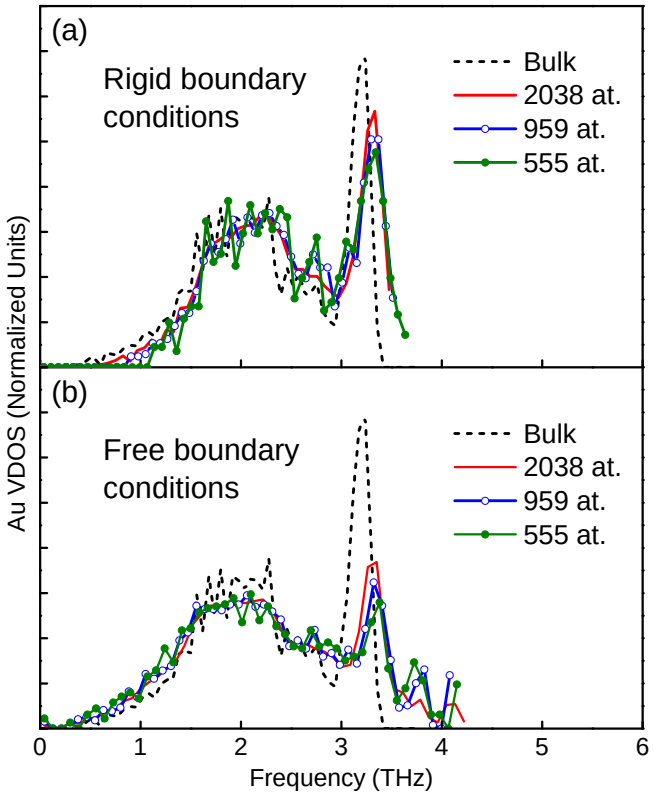

Fig. 6 (Color online) Calculated VDOS in bulk gold (black line) and in different spherical gold nanocrystals, with 2038, 959 and 555 atoms) ; a) with "rigid" and b) "free" boundary conditions

In order to ascertain that the corrected Raman spectrum provides a reliable representation of the VDOS in Au NCs, and analyze more precisely the finite-size effects, we have performed atomistic simulations. This allowed to analyze the specific role of surface versus inner atoms on the frequency redistribution of vibrational modes.

The parameters for gold tight-binding potential have been taken from the work of Cleri and Rosato.[46] The phonon modes are obtained from the calculation and diagonalization of the dynamical matrix. The VDOS of bulk gold generated from an isotropic sampling of the Brillouin zone using a periodic boundary cell is reported in Figs 6a and 6b (dotted lines). The shape is very similar to that already reported in Fig. 5a. How-

ever the available semi-empirical potential for Au underestimates by about 20% the maximum phonon frequency. This inadequacy to account for phonon frequencies in gold has been already noted[46] and ascribed to a strong contribution from noncentral many-body forces, that appears to be of increasing importance along the noble metal series. This contribution may be correlated to the different elastic behavior of Au from the other noble metals, Cu and Ag, as observed experimentally.[47] Nevertheless, we will hereby use simulations in order to analyze qualitatively the effects of size and boundary conditions and will not check precise values of the phonon frequencies.

Spherical NCs have been designed with atoms initially placed on a perfect cubic close-packed crystal structure using the bulk cell parameters of the modeled material.[21] Atoms positions are relaxed using a conjugate gradient algorithm. For the lattice dynamics calculations, two limiting cases for the boundary conditions have been considered: the "rigid" boundary conditions where the surface atoms remain fixed as in a static embedding matrix (Fig. 6a), the "free" boundary conditions, corresponding to a free nanoparticle in vacuum (Fig. 6b). Within both conditions, we examined the effect of the reduction of the number of atoms from ∞ (bulk) to 2038 ($D \approx 4.5$ nm), 959 (where the number at surface and volume atoms are almost equal), and finally 555 ($D \approx 2.9$ nm). In both cases one observes that the high frequency part of the DVOS is broadened and shifted versus higher frequency: this can be interpreted as a signature of structural stiffening in nanoparticles.[48] However, only "free" boundary conditions perfectly account for several experimental trends, namely :

(i) the strong intensity decrease of the LA band and its large frequency up-shift

(ii) the excess observed on the low-frequency tail of the TA band

(iii) the appearance of new modes at higher frequency than the bulk cut-off.

This result confirms in Au the fact that surface atoms play a crucial role in lattice dynamics of nanoparticles, in very good agreement with theoretical predictions in Ag.[45] In Fig. 6b, one verifies that the lower the number of atoms, the higher the anomalies (*i.e.* supplementary modes beyond the cut-off and at low frequency). The validity of the linear elastic theory is obviously questionable at the atomic scale, and it remains only reliable for describing Lamb's modes.[21,49]

Contrary to metallic nanoparticles embedded in a dielectric matrix, where interface, disorder and size distribution effects are important, the sample explored here is made of an assembly of monodisperse Au nanocrystals. In this case, the inhomogeneous broadening effect should be negligible. The strong frequency redistribution of vibrational modes in Au NCs may be explained by surface relaxation effects which are known to be extended over a larger range than in other noble metals: the surface stress is higher in Au than in Ag, as suggested by atomistic simulations[50]. The presence of ligands should play a minor role in this frequency redistribution because they vibrate at much higher frequencies than the Au atoms (See Fig. 4).

5.3 Debye temperature in Au NCs

Changes in the VDOS are at the origin of modifications of thermodynamic properties like specific heat, thermal dilatation or entropy because lattice dynamics plays a prominent role at room temperature with regard to the electronic contribution. As an example, we consider here the lattice specific heat at constant volume C_v which can be calculated from the VDOS $g(\nu)$ as follows:[14]

$$C_v = k_B \int_0^\infty g(\nu) \left(\frac{h\nu}{k_B T}\right)^2 \frac{e^{h\nu/k_B T}}{(e^{h\nu/k_B T}-1)^2} d\nu \qquad (6)$$

In a three-dimensional system with $3N_a$ oscillators, the Debye approximation consists in using $g_D(\nu) = 18\pi N_a (h/k_B T_D)^3 \nu^2$ in Eq. (6), for $0 \leq \nu \leq k_B T_D/h$. One gets a universal Debye function $C_{v,D}(T)$ which temperature dependence is simply determined by the so-called Debye temperature, T_D. Using an experimental or theoretical expression of $g(\nu)$ in Eq. (6) an *effective* Debye temperature can be determined by fitting the curve $C_v(T)$ with $C_{v,D}(T)$ where T_D is the only adjustable parameter. From the bulk Au VDOS reported in Fig. 5a,[29] one finds $T_D = 166$ K in good agreement with experiment ($T_D \approx 170$ K).[14] The "experimental" VDOS extracted from the Raman spectrum has been also used in Eq. (6) to analyze the thermal behavior of disordered materials.[51] Using the VDOS experimental spectrum obtained with Au NCs and reported in Fig. 5a, the best fit is obtained with $T_D = 133$ K : this gives a strong lowering of T_D with size reduction, as predicted theoretically.[52]

6 Conclusions

In this work, an experimental investigation of the spectral response in the THz regime of gold nanocrystals has been presented. By simultaneously exploiting optical amplification, plasmon resonance and dark-field geometry for low frequency Raman scattering, accurate signals have been obtained from a single plane of nanocrystals. Their dynamical response has been particularly analyzed for electronic excitations and *bulk* or *surface* atomic vibrations. First, the continuous and broad spectrum observed in SERS spectra has been well accounted for as inelastic scattering by electron-hole excitations. Its enhancement which accompanies the SERS of vibrational modes of ligands at the plasmon resonance testifies the major role of electron-hole excitations in the microscopic mechanisms.

Second, an experimental evaluation of the VDOS in Au NCs has been performed, and then successfully compared with predictions deduced from atomic-scale calculations. In particular, the presence of high frequency modes beyond the cut-off of bulk VDOS is confirmed supporting the hypothesis of an internal strain effect on core atoms. Moreover the departure from the expected frequency-squared behaviour at low frequency observed experimentally is also well accounted for through atomic simulations. The corresponding excess modes are attributed to the increased role of surface atoms. An ensemble of theoretical works published during the last three decades are thus conforted by these experimental results. They show the inadequacy of the continuous elastic medium approximation for describing most of the vibrational modes in nm-sized systems. The implication on the thermodynamics properties has been also examined by calculating the specific heat in Au NCs. It has been shown experimentally that finite-size effect leads to a strong decrease of the effective Debye temperature.

7 Acknowledgments

M.B. thanks the University of Toulouse and Région Midi-Pyrénées for financial support for his PhD. Part of this work was supported by Programme Investissements d'Avenir under the program ANR-11-IDEX-0002-02, reference ANR-10-LABX-0037-NEXT.

References

1 J. H. Hodak, A. Henglein and G. V. Hartland, *J. Chem. Phys.*, 2000, **112**, 5942.
2 M. Kornbluth, A. Nitzan and T. Seideman, *J. Chem. Phys.*, 2013, **138**, 174707.
3 X. Zhang, Y. L. Chen, R.-S. Liu and D. P. Tsai, *Reports Prog. Phys.*, 2013, **76**, 046401.
4 G. Baffou and R. Quidant, *Laser & Photonics Rev.*, 2013, **7**, 171–187.
5 A. Otto, W. Akemann and A. Pucci, *Isr. J. Chem.*, 2006, **46**, 307–315.
6 G. V. Hartland, *Phys. Chem. Chem. Phys.*, 2004, **6**, 5263.
7 H. E. Sauceda, D. Mongin, P. Maioli, A. Crut, M. Pellarin, N. D. Fatti, F. Vallée and I. L. Garzón, *J. Phys. Chem. C*, 2012, **116**, 25147–25156.
8 E. Duval, A. Boukenter and B. Champagnon, *Phys. Rev. Lett.*, 1986, **56**, 2052–2055.
9 H. Portales, L. Saviot, E. Duval, M. Fujii, S. Hayashi, N. Del Fatti and F. Vallee, *J. Chem. Phys.*, 2001, **115**, 3444.
10 B. Stephanidis, S. Adichtchev, S. Etienne, S. Migot, E. Duval and A. Mermet, *Phys. Rev. B*, 2007, **76**, 121404.
11 H. Portales, N. Goubet, L. Saviot, S. Adichtchev, D. B. Murray, A. Mermet, E. Duval and M.-P. Pileni, *Proc. Natl. Acad. Sci. U. S. A.*, 2008, **105**, 14784–9.
12 H. Portalès, N. Goubet, L. Saviot, P. Yang, S. Sirotkin, E. Duval, A. Mermet and M.-P. Pileni, *ACS Nano*, 2010, **4**, 3489–97.
13 H. Lamb, *Proc. London Math. Soc.*, 1882, **s1-13**, 189–212.
14 C. Kittel, *Introduction to Solid State Physics*, Wiley, 2004, p. 704.
15 N. M. Sangeetha, N. Decorde, B. Viallet, G. Viau and L. Ressier, *J. Phys. Chem. C*, 2013, **117**, 1935–1940.
16 C. Farcau, N. M. Sangeetha, N. Decorde, S. Astilean and L. Ressier, *Nanoscale*, 2012, **4**, 7870–7.
17 R. Carles, C. Farcau, C. Bonafos, G. Benassayag, M. Bayle, P. Benzo, J. Groenen and A. Zwick, *ACS Nano*, 2011, **5**, 8774–82.
18 G. Bachelier and A. Mlayah, *Phys. Rev. B*, 2004, **69**, 205408.
19 S. Adichtchev, S. Sirotkin, G. Bachelier, L. Saviot, S. Etienne, B. Stephanidis, E. Duval and A. Mermet, *Phys. Rev. B*, 2009, **79**, 201402.
20 L. Saviot and D. Murray, *Phys. Rev. B*, 2009, **79**, 214101.
21 N. Combe and L. Saviot, *Phys. Rev. B*, 2009, **80**, 035411.
22 L. Saviot, D. B. Murray, E. Duval, A. Mermet, S. Sirotkin and M. d. C. Marco de Lucas, *Phys. Rev. B*, 2010, **82**, 115450.
23 H. Portales, E. Duval, L. Saviot, M. Fujii, M. Sumitomo and S. Hayashi, *Phys. Rev. B*, 2001, **63**, 233402.
24 S. Mahajan, R. M. Cole, J. D. Speed, S. H. Pelfrey, A. E. Russell, P. N. Bartlett, S. M. Barnett and J. J. Baumberg, *J. Phys. Chem. C*, 2010, **114**, 7242–7250.
25 J. Huang, W. Wang, C. J. Murphy and D. G. Cahill, *Proc. Natl. Acad. Sci. U. S. A.*, 2014, **111**, 906–911.
26 A. Zawadowski and M. Cardona, *Phys. Rev. B*, 1990, **42**, 10732–10734.
27 D. Reznik, M. Klein, W. Lee, D. Ginsberg and S.-W. Cheong, *Phys. Rev. B*, 1992, **46**, 11725–11729.
28 Y. S. Ponosov and S. V. Streltsov, *Phys. Rev. B*, 2012, **86**, 045138.
29 J. Lynn, H. Smith and R. Nicklow, *Phys. Rev. B*, 1973, **8**, 3493–3499.
30 M. Beversluis, A. Bouhelier and L. Novotny, *Phys. Rev. B*, 2003, **68**, 115433.
31 E. Dulkeith, T. Niedereichholz, T. Klar, J. Feldmann, G. von Plessen, D. Gittins, K. Mayya and F. Caruso, *Phys. Rev. B*, 2004, **70**, 205424.
32 M. Geneviève, C. Vieu, R. Carles, A. Zwick, G. Brière, L. Salomé and E. Trévisiol, *Microelectron. Eng.*, 2007, **84**, 1710–1713.
33 C. Farcau and S. Astilean, *Chem. Commun.*, 2011, **47**, 3861–3.
34 I. Sow, J. Grand, G. Lévi, J. Aubard, N. Félidj, J.-C. Tinguely, A. Hohenau and J. R. Krenn, *J. Phys. Chem. C*, 2013, **117**, 25650–25658.
35 R. Carles, A. Zwick, M. Renucci and J. Renucci, *Solid State Commun.*, 1982, **41**, 557–560.
36 H. Richter, Z. Wang and L. Ley, *Solid State Commun.*, 1981, **39**, 625–629.
37 R. Shuker and R. Gammon, *Phys. Rev. Lett.*, 1970, **25**, 222–225.
38 A. Zwick and R. Carles, *Phys. Rev. B*, 1993, **48**, 6024–6032.
39 A. Fontana, F. Rossi, G. Viliani, S. Caponi, E. Fabiani, G. Baldi, G. Ruocco and R. D. Maschio, *J. Phys. Condens. Matter*, 2007, **19**, 205145.
40 V. Crupi, A. Fontana, M. Giarola, S. Longeville, D. Majolino, G. Mariotto, A. Mele, A. Paciaroni, B. Rossi, F. Trotta and V. Venuti, *J. Phys. Chem. B*, 2014, **118**, 624–33.
41 W. Spengler, R. Kaiser, A. Christensen and G. Muller-Vogt, *Phys. Rev. B*, 1978, **17**, 1095–1101.
42 R. Carles, A. Mlayah, M. Amjoud, A. Reynes and R. Morancho, *Jpn. J. Appl. Phys.*, 1992, **31**, 3511–3514.
43 V. Paillard, P. Melinon, V. Dupuis, J. Perez, A. Perez and B. Champagnon, *Phys. Rev. Lett.*, 1993, **71**, 4170–4173.
44 M. Makowska-Janusik, A. Kassiba, J. Bouclé, J.-F. Bardeau, S. Kodjikian and A. Désert, *J. Phys. Condens. Matter*, 2005, **17**, 5101–5110.
45 A. Kara and T. Rahman, *Phys. Rev. Lett.*, 1998, **81**, 1453–1456.
46 F. Cleri and V. Rosato, *Phys. Rev. B*, 1993, **48**, 22–33.
47 W. Kamitakahara and B. Brockhouse, *Phys. Lett. A*, 1969, **29**, 639–640.
48 Q. F. Gu, G. Krauss, W. Steurer and A. Cervellino, *Phys. Rev. Lett.*, 2008, **100**, 045502.
49 L. Saviot, N. Combe and A. Mlayah, *Phys. Rev. B*, 2012, **85**, 075405.
50 R. Meyer, L. Lewis, S. Prakash and P. Entel, *Phys. Rev. B*, 2003, **68**, 104303.
51 G. Carini, G. Carini, G. DAngelo, G. Tripodo, G. Di Marco, C. Vasi and E. Gilioli, *Phys. Rev. Lett.*, 2013, **111**, 245502.
52 B. Roldan Cuenya, L. K. Ono, J. R. Croy, K. Paredis, A. Kara, H. Hein-

rich, J. Zhao, E. E. Alp, A. T. DelaRiva, A. Datye, E. A. Stach and W. Keune, *Phys. Rev. B*, 2012, **86**, 165406.